Journal of Applied Physics

AIP Publishing

RESEARCH ARTICLE | MAY 08 2023

Structural properties of MBE-grown CdTe (133)B buffer layers on GaAs (211)B substrates with CdZnTe/CdTe superlattice-based dislocation filtering layers

Wenwu Pan ; Shuo Ma ; Xiao Sun ; Shimul Kanti Nath; Songqing Zhang; Renjie Gu ; Zekai Zhang; Lorenzo Faraone ; Wen Lei

Journal of Applied Physics 133, 185301 (2023)
https://doi.org/10.1063/5.0143854

Journal of
Applied Physics

ARTICLE

scitation.org/journal/jap

Structural properties of MBE-grown CdTe (133)B buffer layers on GaAs (211)B substrates with CdZnTe/CdTe superlattice-based dislocation filtering layers

Cite as: J. Appl. Phys. **133**, 185301 (2023); doi: 10.1063/5.0143854
Submitted: 27 January 2023 · Accepted: 23 April 2023 ·
Published Online: 8 May 2023

Wenwu Pan,[1,a)] Shuo Ma,[1] Xiao Sun,[2] Shimul Kanti Nath,[1] Songqing Zhang,[1] Renjie Gu,[1] Zekai Zhang,[1] Lorenzo Faraone,[1] and Wen Lei[1,b)]

AFFILIATIONS

[1] ARC Centre of Excellence for Transformative Meta-Optical Systems (TMOS), Department of Electrical, Electronic and Computer Engineering, The University of Western Australia, Perth, Western Australia 6009, Australia
[2] John de Laeter Center, Curtin University, Perth, Western Australia 6102, Australia

[a)] **Electronic mail:** wenwu.pan@uwa.edu.au
[b)] **Author to whom correspondence should be addressed:** wen.lei@uwa.edu.au

ABSTRACT

The ever-present demand for high-performance HgCdTe infrared detectors with larger array size and lower cost than currently available technologies based on lattice-matched CdZnTe (211)B substrates has fuelled research into heteroepitaxial growth of HgCdTe and CdTe buffer layers on lattice-mismatched alternative substrates with a (211)B orientation. Driven by the large lattice mismatch, the heteroepitaxial growth of (Hg)CdTe can result in (133)B-orientated material, which, however, has been less explored in comparison to (211)B-oriented growth. Herein, we report on the structural properties of heteroepitaxially grown single-crystal II–VI CdTe (133)B-oriented buffer layers on III–V GaAs (211)B substrates. Azimuthal-dependent x-ray double-crystal rocking curve measurements for the CdTe buffer layers show that the full-width at half-maximum value obtained along the GaAs $[\bar{1}11]$ direction is narrower than that obtained along the GaAs $[01\bar{1}]$ direction, which is presumably related to the in-plane anisotropic structural characteristics of the grown CdTe layers. By incorporating strained CdZnTe/CdTe superlattice-based dislocation filtering layers (DFLs), a significant improvement in material quality has been achieved in (133)B-orientated CdTe buffer layers, including a reduced etch pit density in the low-$10^5\,\mathrm{cm}^{-2}$ range and improved surface roughness. These results indicate that the CdTe (133)B DFL buffer layer process is a feasible approach for growing high-quality CdTe and HgCdTe materials on large-area, low-cost alternative substrates.

INTRODUCTION

The II–VI (Hg)(Cd)(Zn)Te-based semiconductors are significant technological materials with a wide range of applications in high-performance infrared (IR) sensing/imaging, radiation detectors, and solar cells.[1] In particular, HgCdTe is well established as a material system with a widely tunable working wavelength range (1–30 μm), high absorption coefficient, long carrier lifetimes, and high carrier mobilities, which have established it as the leading semiconductor for fabricating high-performance infrared detectors and imaging focal plane arrays (FPAs).[2] In addition, HgCdTe epilayers grown by molecular beam epitaxy (MBE) have emerged as attractive materials for developing integrated chem/biomedical sensing systems,[3] terahertz photonic systems,[4] and topological electronics.[5,6] CdZnTe is also a representative II–VI compound semiconductor that has promising applications in solar cells and radiation detectors.[7,8] In particular, $\mathrm{Cd_{0.96}Zn_{0.04}Te}$ (CZT) has long been the baseline substrate for lattice-matched epitaxial growth of high-quality HgCdTe for fabricating high-performance IR FPAs.[9]

However, due to the soft and brittle nature of II–VI materials, CZT substrates are generally of lower crystal quality, smaller area, and much higher cost in comparison to other Group IV and III–V substrates.[10] It is primarily substrate-related issues that have prevented HgCdTe and CdZnTe from being more widely adopted in applications demanding compact, sensitive, and lower-cost optoelectronic devices.

To overcome these limitations, much attention has been paid to the heteroepitaxy of II–VI (Hg)(Cd)(Zn)Te semiconductors on lattice-mismatched alternative substrates, such as Si, Ge, GaAs, and GaSb.[2,11–14] In the heteroepitaxy of HgCdTe, an intermediate CdTe buffer layer is commonly interposed between these alternative substrates and HgCdTe to accommodate the large lattice and CTE (coefficient of thermal expansion) mismatches allowing the epitaxial HgCdTe layer to grow with fewer threading dislocation density (TDD).[15–18] In addition, the buffer layer also plays an important role in blocking threading dislocations (TDs) generated from the mismatched CdTe buffer/substrate interface. However, due to the limited dislocation blocking efficiency of the CdTe buffer layer and the slight lattice mismatch between HgCdTe and CdTe (∼0.24%), none of these approaches yields HgCdTe with TDD (etch pit density—EPD of mid-10^6 to low-10^7 cm^{-2}), detector performance, and FPA operability comparable to those grown on lattice-matched CdZnTe, especially for long-wave IR detectors in which EPD levels below mid-10^5 cm^{-2} are required.[19] Recently, we reported on a CdTe-based buffer layer utilizing strained CdZnTe/CdTe superlattice-based dislocation filtering layers (DFLs) that can reduce the EPD of CdTe (211)B grown on GaAs (211)B from low-10^7 to low-10^6 cm^{-2} (5×10^5 cm^{-2} for the best layer) as well as reduce the lattice mismatch between the CdTe buffer layer and HgCdTe device layer.[18,20] The superlattice-based strained layers create a mismatch stress field that induces a lateral force on TD segments, causing them to glide and annihilate at the superlattice interfaces. In addition to the DFL designs and growth conditions that we have previously investigated, the specific crystal growth orientations can also affect the structural properties and dislocation filtering efficiency, which are worth exploring.[21]

Epitaxially grown layers generally take up the same orientation as the substrate, and this is especially true for lattice-matched epitaxy. MBE-grown HgCdTe layers with low-index surface orientations such as (001) and (111) have been found to suffer from growth issues such as requiring high Hg flux and the formation of hillocks, facets, twins, etc.[22] Although the most common growth orientation used to minimize these issues for growing high-quality HgCdTe is (211)B, it should be noted that the heteroepitaxy of CdTe on lattice-mismatched substrates has the capability of dual epitaxy.[23] Of particular interest is the fact that both CdTe (211)B and CdTe (133)B can be grown on (211)B-orientated Si, Ge, and GaAs substrates.[24–26] Zanatte *et al.* demonstrated that the high index (133)B surface appears not to be detrimental to the subsequent MBE growth of (133)B-orientated HgCdTe in terms of structural quality and surface morphology.[26] Previous studies have tended to focus on (211)B-orientated HgCdTe layers,[11,18] while detailed studies on characterizing heteroepitaxially grown CdTe (133)B layers as well as procedures for lowering their dislocation density are rather limited.

In this work, (133)B-orientated single-crystal CdTe buffer layers, both without and with strained CdZnTe/CdTe superlattice-based DFLs, have been grown on GaAs (211)B substrates by MBE. Transmission electron microscopy (TEM), high-resolution x-ray diffraction (XRD), and atomic force microscopy (AFM) have been employed to study the structural properties of the CdTe (133)B DFL buffer layers grown on GaAs (211)B substrates. In addition, both EPD measurements and scanning electron microscopy-based cathodoluminescence (SEM-CL) have been used to characterize the dislocation filtering efficiency of the DFLs. Our preliminary experimental results confirm that the DFL buffer layer process is quite effective for the (133)B-orientated CdTe layers in terms of defect filtering and reduction.

RESULTS AND DISCUSSIONS

Figure 1(a) schematically shows the orientation relationship between CdTe epilayers with different orientations and the GaAs (211)B substrates. The dual epitaxy of CdTe on GaAs can be understood by the fact that the tetrahedral bond network continues from (211) GaAs to (133) CdTe with less distortion than the case for a (211) epilayer.[23] Specifically, the lattice mismatch remains 14.6% for the $[01\bar{1}]$ GaAs // $[01\bar{1}]$ CdTe direction but is reduced to 0.3% for the $[\bar{1}11]$ GaAs // $[\bar{6}11]$ CdTe direction. Some previous studies describing the control of the two CdTe orientations have been reported, in which the growth temperatures were found to have a strong influence on the observed orientations.[25,27,28] Recent growth simulations based on molecular dynamics have indicated that the large reduction of strain and dislocation energies can initiate (133) oriented growth on lattice-mismatched (211) substrates,[29] which is consistent with the growth results that higher growth temperatures favor the formation of (133) oriented material. Figure 1(b) shows a typical sample structure for a CdTe buffer layer with five sets of superlattice-based DFLs grown in a Riber 32P MBE system on a 2-in. GaAs (211)B substrate. The growth temperature was estimated to be ∼270 °C based on thermocouple reading of the sample manipulator. A detailed description of the growth process/parameters for the CdTe DFL buffers can be found in our previous report.[18] The growth process/parameters consistently resulted in (211)B-dominated CdTe epilayers. Unexpectedly, two consecutive growths resulted in CdTe (133)B layers, which probably resulted from changes in actual substrate temperature during growth. For the (133)B buffers both with and without DFL, their XRD patterns were dominated by CdTe (133) reflection at $\omega = 31.5°$, and no other peaks were observed, indicating that no twinned crystalline CdTe layers were grown. In contrast, the XRD patterns for CdTe (211)B layers on GaAs (211)B substrates were typically dominated by (422) reflection, which is tilted toward the $[\bar{1}11]$ crystallographic direction with respect to the normal GaAs (211) surface, as illustrated in Fig. 1(a). Fourier-transform IR spectroscopy was used to measure the buffer layer thickness, and no obvious growth rate changes (<15%) were found for growth in the (133) orientation as in comparison to CdTe layers with (211) orientation. TEM was used to examine the CdTe buffer layer structure in detail. The selected area electron diffraction (SAED) pattern shown in Fig. 1(c) confirms that the CdTe DFL buffer layer was grown as a single crystal with (133) surface orientation. In spite of the

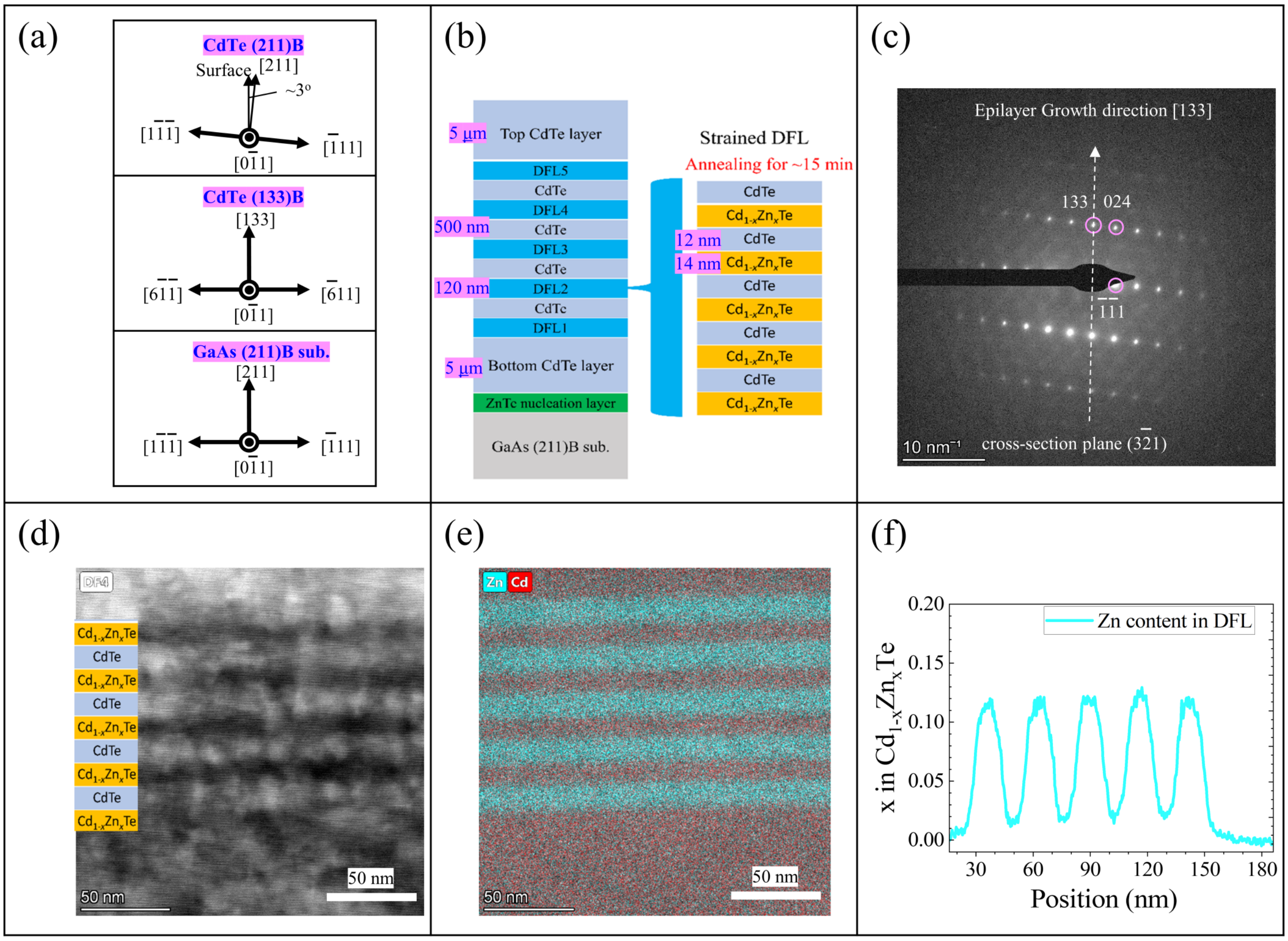

FIG. 1. Structural properties of a (133) orientated CdTe buffer layer. (a) Schematic for orientation relationship between (211) GaAs substrate and CdTe epilayers with different orientations; (b) schematic sample structure for MBE growth of CdTe buffer layers with CdZnTe/CdTe superlattice-based DFLs; (c) cross-sectional SAED (selected area electron diffraction) pattern observed for the (133) orientated buffer layer; (d) cross-sectional TEM image collected for a DFL including five periods of $Cd_{1-x}Zn_xTe$/CdTe with thicknesses of ~14/~12 nm, respectively, as confirmed by the chemical composition map shown in (e); (f) the averaged Zn content (x) profile across the DFL.

surface roughness [Fig. 1(d)] caused by ion-milling damage during TEM sample preparation,[30,31] well-defined interfaces and uniform chemical compositions within individual superlattice layers were confirmed by EDS (energy dispersive spectroscopy) for elemental mapping in TEM, as shown in Fig. 1(e). As indicated in Fig. 1(f), the average Zn content (x) in the CdZnTe layers was measured to be 0.12, which is consistent with the XRD results that will be discussed later.

Apart from TEM measurements, AFM and EPD measurements were also utilized to characterize and evaluate the MBE growth and material quality of the CdTe (133) buffer layers, both with and without the incorporation of DFLs. As shown in the AFM images in Figs. 2(a) and 2(b), the root mean squared (RMS) surface roughness of the CdTe (133) DFL layer is measured to be 3 nm over an area of $10 \times 10\,\mu m^2$, which is lower than the 8 nm measured on the (133) oriented CdTe-only reference sample. EPD measurements were undertaken by using a 60 s Everson etch on both samples.[32] From the optical images shown in Figs. 2(c) and 2(d), the EPD for the uppermost CdTe with DFLs was measured to be $\sim 3 \times 10^5\,cm^{-2}$, approximately 20 times lower than that of the single-layer CdTe reference sample, with an EPD of $\sim 7 \times 10^6\,cm^{-2}$, suggesting the efficient dislocation filtering effect of the strained CdZnTe/CdTe superlattice layers. The EPD levels measured for the CdTe (133) layers are comparable to the best results we had obtained previously on CdTe layers with (211)B orientation.[18] This can be attributed to the reduced lattice mismatch along $[\bar{6}11]$ CdTe // $[\bar{1}11]$ GaAs. However, it is worth noting that the Everson etchant is generally used for CdTe (211)B layers;[32] thus, the EPD

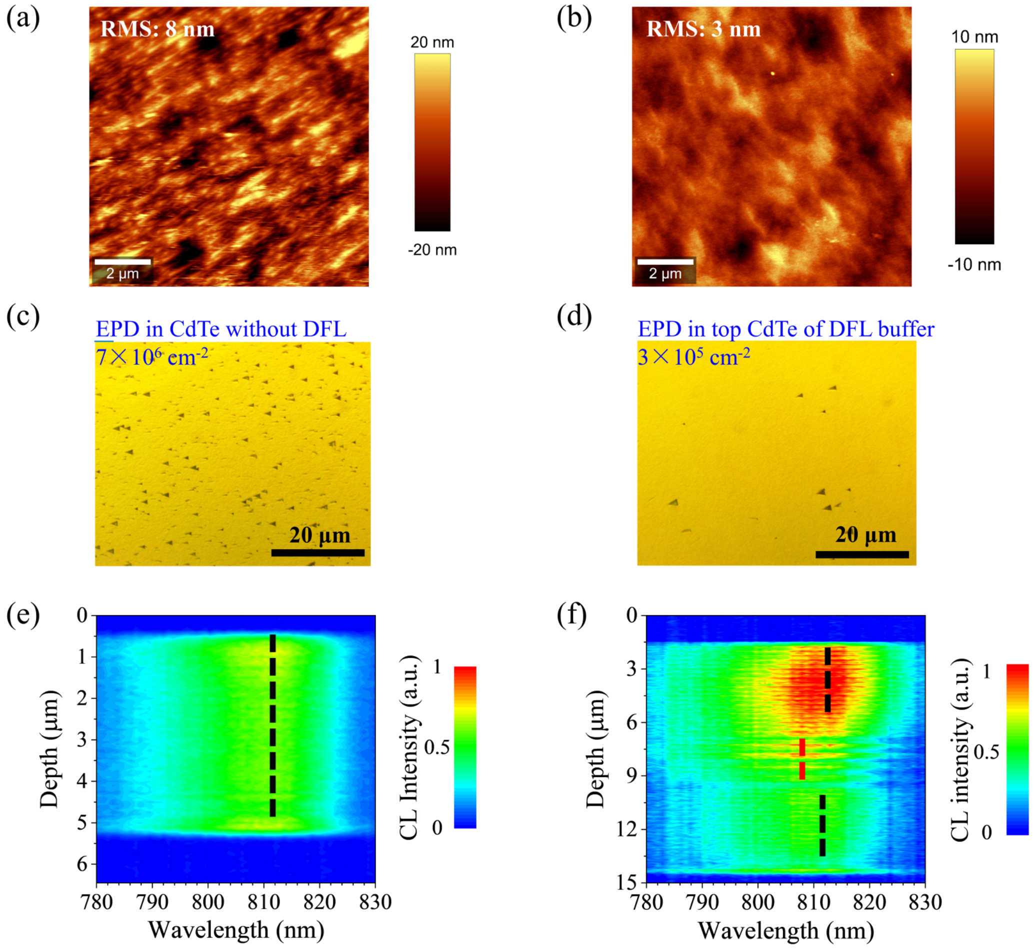

FIG. 2. (a) and (b) Surface AFM images, (c) and (d) EPD measurements of the uppermost CdTe surface, and (e) and (f) depth-dependence of cross-sectional CL of CdTe (133)B buffers. (a), (c), and (e) are for an ~5 μm thick single CdTe (133) layer without DFL for reference and (b), (d), and (f) are for an ~13 μm thick CdTe DFL buffer layer that includes the CdZnTe/CdTe superlattice-based DFLs.

values obtained for the CdTe layers with different orientations may not be directly comparable.[33,34] The validity of EPD measurements for (133) (Hg)CdTe layers with the use of the etchants used for (211) (Hg)CdTe layers needs to be further investigated.

As compared with the observation of almost uniform CL intensity across the thickness for the (133) CdTe without DFL [Fig. 2(e)], enhanced CL intensity is observed for the upper CdTe layer incorporating DFLs compared to the bottom CdTe layer, as shown in Fig. 2(f). In addition, five CL quenching areas are observed along the growth direction for the CdTe DFL sample, corresponding to the 120 nm thick DFL layers separated by the 500 nm thick CdTe spacers. This suggests that TDs are converted into misfit dislocations (MDs) that are confined to the interfaces of the superlattice layers.[35] This is an indication of dislocation filtering, which facilitates non-radiative recombination and, hence, decreases the CL efficiency of the DFL layers while increasing CL emission from the upper CdTe layer. The observation of a blueshift of the CL peak in Fig. 2(f) further confirms the compressive strain for the CdTe layers in/near the DFL region, which is consistent with the XRD results and will be discussed in the following.

Besides confirming the dislocation filtering effect, it is important to evaluate the lattice strain present in the (133) oriented CdTe DFL buffers, which serves as the driving force for dislocating filtering. XRD reciprocal space mappings (RSMs) with x-ray beam direction aligned with the $[0\bar{1}1]$ direction of the substrate were carried out. Figures 3(a) and 3(b) show the XRD-RSMs around the asymmetric (115) and symmetric (133) reflections measured for the (133) CdTe DFL buffer layer, respectively. In each RSM, clear superlattice-related interference fringes (satellite peaks from the superlattice layers) are observed, indicating that sharp CdZnTe/CdTe superlattice interfaces have been achieved. In Fig. 3(a), negligible lattice tilting (α) of the (133) plane with respect to the

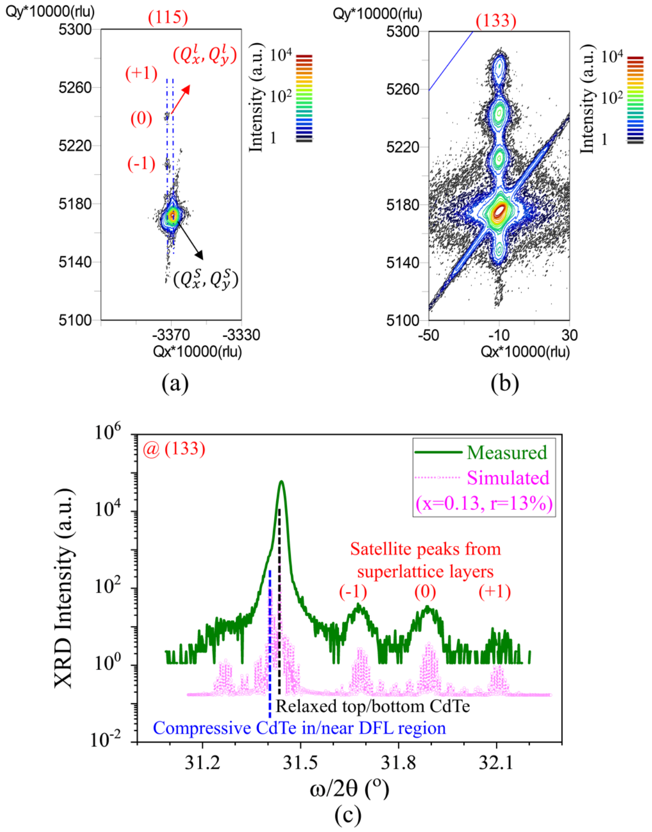

FIG. 3. XRD characterization of the (133)B-orientated CdTe DFL buffer layer grown on GaAs (211)B. (a) RSMs of asymmetric (115) reflection and (b) symmetric (133) reflection. In each RSM, the dominant bottom peak corresponds to the relaxed top CdTe layer, and the upper features consist of several interference fringes corresponding to the strained CdZnTe/CdTe superlattice-based DFLs. The vertical lines (blue dashes) in asymmetric (115) RSM represent reciprocal lattice points where the parallel lattice constant of the CdZnTe is equal to that of the compressively strained CdTe in/near the DFL region but slightly less than that of the relaxed top CdTe layer: that is, a coherently strained superlattice. (c) (133) ω−2θ diffraction spectrum measured for the CdTe DFL buffer and the theoretical simulation. The dominant bottom peak corresponds to the relaxed top/bottom CdTe layer, and the nearby sub-peak with lower intensity corresponds to the CdTe layers in/near the DFL region. The curves are shifted vertically for better visibility.

TABLE I. Material parameters used in the XRD analysis for calculating the Zn content, x, in $Cd_{1-x}Zn_xTe$ layers.

	CdTe		ZnTe	
Lattice constant (a)	0.6483 nm		0.6105 nm	
Elastic constants (C_{ij}, GPa)	$C_{11} = 53.5$, $C_{12} = 36.8$, $C_{44} = 19.9$		$C_{11} = 71.3$, $C_{12} = 40.7$, $C_{44} = 31.2$	
Orientation (hkl)	R^B	ν	R^B	ν
(100)	1.3757	0.4075	1.1417	0.3634
(011)	0.9539	0.3229	0.7511	0.2730
(111)	0.8447	0.2969	0.6508	0.2455
(211)	0.9539	0.3229	0.7511	0.2730
(133)	0.9208	0.3153	0.7207	0.2649

substrate surface is observed, which can be estimated by the expression $\alpha = \tan^{-1}(Q_x/Q_y)$, where Q_x and Q_y are the coordinates of the symmetric reflection of the epilayer.

As indicated by the CL results, CdTe layers in/near the DFL region appear to be compressively strained to partially compensate the large tensile strain in the $Cd_{1-x}Zn_xTe$ layers. Similar coherent growth has been previously observed in our CdTe (211) DFL buffer layers and in other material systems such as InGaN/GaN superlattice structures grown on GaN.[20,36] From the RSM results, as denoted in Fig. 3(a), parallel mismatch $\left(m_{//} = \frac{Q_x^l - Q_x^S}{Q_x^l}\right)$ of $m_{//} = 0.098\%$ and perpendicular mismatch $\left(m_{\perp} = \frac{Q_y^l - Q_y^S}{Q_y^l}\right)$ of $m_{\perp} = 1.34\%$ between the tensile-strained CdZnTe layers and the relaxed CdTe layer can be deduced. Correspondingly, the in-plane lattice mismatch between the DFL region and HgCdTe was estimated to be reduced to 40% of that in conventional CdTe buffer/HgCdTe (0.24%). Note that the compressively strained CdTe layers in/near the DFL region will lead to a spread in the x-ray double-crystal rocking curve full-width at half-maximum (FWHM) values measured for the top CdTe layers for thicknesses less than approximately 7 μm.

Considering the biaxial Poisson ratio (R^B) for the (133) orientated $Cd_{1-x}Zn_xTe$, as listed in Table I, the x-value and the relaxation (r) of the CdZnTe superlattice layers with respect to the relaxed CdTe bottom/top layer are determined to be x = 0.13 and r = 13%, respectively. In addition, as shown in Fig. 3(c), the structural parameters of CdTe DFL buffers can be further confirmed by comparing the measured and simulated XRD curves within X'PERT EPITAXY software (PANalytical, Version 4.2). From the fitting for the CdTe (133) DFL buffer layer, the thicknesses of the CdZnTe/CdTe layers are derived to be 14/12 nm, respectively, which are in good agreement with cross-sectional TEM measurements.

Within the XRD analysis, as listed in Table I, well-established lattice parameters (a) and effective uniaxial Poisson ratios (ν) for binary ZnTe and CdTe were used. It is important to note that the ν (R^B), which generally defines the ratio of transverse strain (the out-of-plane strain) to the axial strain (the in-plane biaxial strain), is dependent on the surface orientation index (hkl). Thus, inaccuracies in its value will affect the accuracy of compositions derived from the mismatches. For binary ZnTe and CdTe with different orientations, ν can be estimated by the biaxial Poisson ratio (R^B) from the expressions $\nu = R^B/(2 + R^B)$ and $R^B = \frac{2[c_{12}(h^4+k^4+l^4)+(c_{11}+c_{12}-2c_{44})(h^2k^2+h^2l^2+k^2l^2)]}{c_{12}(h^4+k^4+l^4)+2(c_{11}+2c_{44})(h^2k^2+h^2l^2+k^2l^2)}$, where c_{11}, c_{12}, and c_{44} are the elastic stiffness parameters for the binary materials.[37,38] For $Cd_{1-x}Zn_xTe$, the parameters of a and ν are x-dependent and can be calculated using Vegard's law, i.e., using simple linear interpolation between the binary compounds of CdTe and ZnTe.[39,40] As listed in Table I, the calculated ν and R^B would be helpful for evaluating the Zn content in CdZnTe/CdTe DFL structures for various orientations.

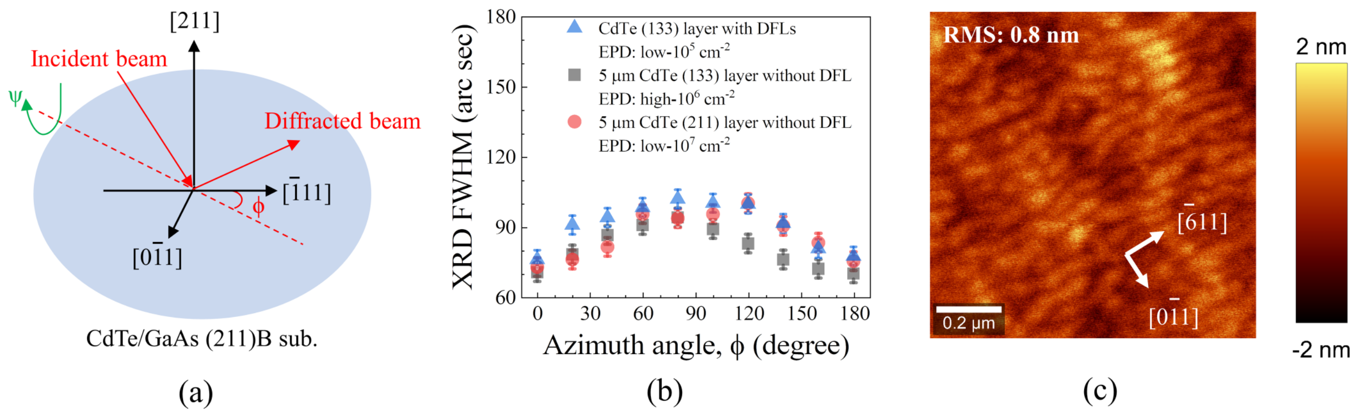

(a) (b) (c)

FIG. 4. (a) Experimental geometry of the azimuthal-dependent XRD measurement, defining the azimuth angle as zero when the projection of the incident beam is parallel to the $[\bar{1}11]$ GaAs substrate axis; (b) azimuth angle dependence of the FWHMs of the (422) ω rocking curve for the (211) orientated CdTe buffer and (133) ω rocking curves for the (133) CdTe buffers with and without DFL. (c) An AFM image of the (133) CdTe DFL buffer surface. The sample shows arrowhead-like features along the CdTe $[\bar{6}11]$ direction (GaAs $[\bar{1}11]$ direction). The root mean square (RMS) roughness of the (133) CdTe DFL buffer layer is 0.8 nm over an area of $1 \times 1\,\mu m^2$.

The XRD FWHM extracted from the x-ray rocking curves of the symmetric diffraction peak has been widely used to screen epilayers in terms of defect density. However, other factors, such as strain and experimental geometry for XRD measurements,[15] that may affect the results are often ignored. For example, for the CdTe buffer layer grown with DFLs, the compressively strained CdTe in/near the DFL region and misfit dislocations in DFLs can lead to significant FWHM spreading due to the relatively large sampling depth of ∼7 μm.[18] As expected, the FWHMs of the rocking curves for symmetric (133) reflections obtained for the CdTe (133) layers with and without DFL are similar, regardless of their large difference in EPD levels. In addition, due to the tilted growth of (211) CdTe on (211) GaAs, the symmetric (422) ω rocking curve and the associated FWHM can only be obtained with x-ray incidence direction parallel to the GaAs $[\bar{1}11]$ if the default wafer tilting angle of $\psi = 0$ was not changed. However, this is not the case for the non-tilted (133) CdTe layers, and it is important to note that the x-ray incidence direction should be specified when comparing the crystalline quality based on XRD FWHM results.

Given the above discussion, x-ray rocking curves for the symmetric diffraction peak of CdTe for various x-ray incidence directions were measured for the CdTe layers with (133) and (211) orientations, as schematically shown in Fig. 4(a). The azimuth angle (ϕ) is defined as zero when the x-ray incidence direction is parallel to $[\bar{1}11]$ of the GaAs substrate. Note that, in the measurements for the (211) CdTe buffer layer, it is essential to adjust ψ to pick up the (422) reflection when $\phi \neq 0$. Overall, what stands out from Fig. 4(b) is that for all three CdTe buffer layers studied, their full-width at half-maximum (FWHM) values strongly depend on the x-ray incidence direction. Similar levels of anisotropic ω FWHM distribution are observed regardless of their different EPD levels and orientations; i.e., the FWHM value measured with $\phi = 0$ is about 70 arc sec, whereas that measured with $\phi = 90$ is around 100 arc sec. AFM measurements for the (133) CdTe DFL buffer layer grown on GaAs gave a small RSM of 0.8 nm over an area of $1 \times 1\,\mu m^2$ but also showed a large anisotropy in the surface microstructures, as shown in Fig. 4(c). The grains are larger in size along the $[\bar{1}11]$ direction compared to the $[01\bar{1}]$ direction, which is correlated with the observed azimuthal-dependent XRD FWHM values. Although the observation of azimuthal-dependent XRD FWHM has been reported for heteroepitaxial semiconductors, including several III–V Zincblende and Wurtzite semiconductors,[41,42] there are few reports in the literature for II–VI semiconductors. Several mechanisms were found to lead to observable azimuthal variation in the rocking curve for symmetric x-ray reflections, including an anisotropic distribution of the densities of microstructures such as threading dislocations and stacking faults present in epilayers; anisotropic wafer bending due to the thermal mismatch between the epilayer and substrate, etc. Further comparisons of the azimuthal-dependent XRD FWHM and the associated mechanisms in various epitaxial II–VI (Hg)CdTe systems, including HgCdTe/CdZnTe, are worth investigating in the future.

SUMMARY AND CONCLUSIONS

In summary, this study has demonstrated a dramatic improvement in material quality and corresponding EPD of (133) orientated CdTe buffer layers grown on lattice-mismatched GaAs (211)B substrates as a direct result of incorporating tensile-strained CdZnTe/CdTe superlattice-based DFLs. The results suggest that the beneficial effects of CdZnTe/CdTe DFLs are not limited to (211)B orientation but may be applied to the growth of CdTe buffer layers with other directions such as (001) and (111), which are widely adopted in optoelectronic devices. Similar to the CdTe (211)B layers, XRD-RSMs and CL measurements have revealed that the DFL region is coherently grown, leading to a spread in XRD FWHM but with better in-plane lattice-matching to HgCdTe, in comparison to conventional single-layer CdTe buffer layers on GaAs. The incorporation of DFLs leads to reduced EPD and enhanced CL emission in the relaxed top CdTe layer. The rocking curves of the symmetric reflections for both the (133) and (211) orientated CdTe layers are found to be anisotropically broadened with FWHM of ~70 arc sec along the GaAs $[\bar{1}11]$ direction and ~100 arc sec along the GaAs $[01\bar{1}]$ direction, which is correlated with the observed anisotropic surface morphology.

ACKNOWLEDGMENTS

This work was supported by the Australian Research Council (Nos. DP200103188 and CE200100010) and a Research Impact Grant from the University of Western Australia (UWA). Facilities used in this work are supported by the WA node of the Australian National Fabrication Facility (ANFF) and the Centre for Microscopy, Characterization and Analysis (CMCA) at UWA. Shimul Kanti Nath acknowledges the support of the Forrest Prospect Fellowship awarded by the Forrest Research Foundation, Australia. This work was supported by John de Laeter Centre, Curtin University, and Curtin Faculty of SAE R&DC Small Grant.

AUTHOR DECLARATIONS

Conflict of Interest

The authors have no conflicts to disclose.

Author Contributions

Wenwu Pan: Conceptualization (lead); Data curation (equal); Formal analysis (lead); Investigation (lead); Methodology (lead); Resources (equal); Software (equal); Validation (lead); Visualization (lead); Writing – original draft (lead). **Shuo Ma:** Methodology (supporting). **Xiao Sun:** Methodology (supporting). **Shimul Kanti Nath:** Methodology (supporting). **Songqing Zhang:** Methodology (supporting). **Renjie Gu:** Methodology (supporting). **Zekai Zhang:** Methodology (supporting). **Lorenzo Faraone:** Funding acquisition (lead); Project administration (equal); Supervision (equal); Writing – review & editing (equal). **Wen Lei:** Project administration (equal); Supervision (equal); Writing – review & editing (equal).

DATA AVAILABILITY

The data that support the findings of this study are available from the corresponding author upon reasonable request.

REFERENCES

[1] G. Dhanaraj, K. Byrappa, V. Prasad, and M. Dudley, *Springer Handbook of Crystal Growth* (Springer, 2010), Vol. 2.

[2] W. Lei, J. Antoszewski, and L. Faraone, Appl. Phys. Rev. **2**, 041303 (2015).

[3] X. Wang, J. Antoszewski, G. Putrino, W. Lei, L. Faraone, and B. Mizaikoff, Anal. Chem. **85**, 10648–10652 (2013).

[4] S. Ruffenach, A. Kadykov, V. V. Rumyantsev, J. Torres, D. Coquillat, D. But, S. S. Krishtopenko, C. Consejo, W. Knap, S. Winnerl, M. Helm, M. A. Fadeev, N. N. Mikhailov, S. A. Dvoretskii, V. I. Gavrilenko, S. V. Morozov, and F. Teppe, APL Mater. **5**, 035503 (2017).

[5] B. A. Bernevig, T. L. Hughes, and S.-C. Zhang, Science **314**, 1757–1761 (2006).

[6] F. Teppe, M. Marcinkiewicz, S. S. Krishtopenko, S. Ruffenach, C. Consejo, A. M. Kadykov, W. Desrat, D. But, W. Knap, J. Ludwig, S. Moon, D. Smirnov, M. Orlita, Z. Jiang, S. V. Morozov, V. I. Gavrilenko, N. N. Mikhailov, and S. A. Dvoretskii, Nat. Commun. **7**, 12576 (2016).

[7] T. E. Schlesinger, J. E. Toney, H. Yoon, E. Y. Lee, B. A. Brunett, L. Franks, and R. B. James, Mater. Sci. Eng. R: Rep. **32**, 103–189 (2001).

[8] Y. Zhao, M. Boccard, S. Liu, J. Becker, X. H. Zhao, C. M. Campbell, E. Suarez, M. B. Lassise, Z. Holman, and Y.-H. Zhang, Nat. Energy **1**(6), 16067 (2016).

[9] A. Rogalski, J. Antoszewski, and L. Faraone, J. Appl. Phys. **105**, 091101 (2009).

[10] R. Singh, S. Velicu, J. Crocco, Y. Chang, J. Zhao, L. A. Almeida, J. Markunas, A. Kaleczyc, and J. H. Dinan, J. Electron. Mater. **34**, 885–890 (2005).

[11] J. D. Benson, L. O. Bubulac, P. J. Smith, R. N. Jacobs, J. K. Markunas, M. Jaime-Vasquez, L. A. Almeida, A. Stoltz, J. M. Arias, G. Brill, Y. Chen, P. S. Wijewarnasuriya, S. Farrell, and U. Lee, J. Electron. Mater. **41**, 2971–2974 (2012).

[12] W. Lei, R. J. Gu, J. Antoszewski, J. Dell, and L. Faraone, J. Electron. Mater. **43**, 2788–2794 (2014).

[13] W. Lei, R. J. Gu, J. Antoszewski, J. Dell, G. Neusser, M. Sieger, B. Mizaikoff, and L. Faraone, J. Electron. Mater. **44**, 3180–3187 (2015).

[14] T. J. De Lyon, R. D. Rajavel, B. Z. Nosho, S. Terterian, M. L. Beliciu, P. R. Patterson, D. T. Chang, M. F. Boag-O'Brien, B. T. Holden, and R. Jacobs, J. Electron. Mater. **39**, 1058–1062 (2010).

[15] J. D. Benson, R. N. Jacobs, J. K. Markunas, M. Jaime-Vasquez, P. J. Smith, L. A. Almeida, M. Martinka, M. F. Vilela, and U. Lee, J. Electron. Mater. **37**, 1231–1236 (2008).

[16] W. Lei, Y. L. Ren, I. Madni, and L. Faraone, Infrared Phys. Technol. **92**, 96–102 (2018).

[17] W. W. Pan, R. J. Gu, Z. K. Zhang, J. L. Liu, W. Lei, and L. Faraone, J. Electron. Mater. **49**, 6983–6989 (2020).

[18] W. W. Pan, R. J. Gu, Z. K. Zhang, W. Lei, G. A. Umana-Membreno, D. J. Smith, J. Antoszewski, and L. Faraone, J. Electron. Mater. **51**, 4869–4883 (2022).

[19] S. M. Johnson, D. R. Rhiger, J. P. Rosbeck, J. M. Peterson, S. M. Taylor, and M. E. Boyd, J. Vac. Sci. Technol. B **10**, 1499 (1992).

[20] W. Pan, S. K. Nath, S. Ma, R. Gu, Z. Zhang, L. Fu, L. Faraone, and W. Lei, J. Appl. Phys. **131**, 205304 (2022).

[21] I. Salehinia and D. F. Bahr, Int. J. Plast. **52**, 133–146 (2014).

[22] J. W. Garland and S. Sivananthan, *Springer Handbook of Crystal Growth* (Springer, 2010), p. 1069.

[23] Y. Nakamura, N. Otsuka, M. D. Lange, R. Sporken, and J. P. Faurie, Appl. Phys. Lett. **60**, 1372–1374 (1992).

[24] S. M. Johnson, J. B. James, W. L. Ahlgren, W. J. Hamilton, and M. Ray, Appl. Phys. Lett. **59**, 2055 (1991).

[25] K. Iso, Y. Gokudan, M. Shiraishi, M. Nishikado, H. Murakami, and A. Koukitu, J. Electron. Mater. **48**, 454–459 (2019).

[26] J. P. Zanatta, P. Duvaut, P. Ferret, A. Million, G. Destefanis, P. Rambaud, and C. Vannuffel, Appl. Phys. Lett. **71**, 2984–2986 (1997).

[27] T. Sasaki, M. Tomono, and N. Oda, J. Vac. Sci. Technol. B **10**, 1399 (1992).

[28] G. J. Gouws and R. J. Muller, J. Electron. Mater. **24**, 1099–1104 (1995).

[29] X. W. Zhou, J. J. Chavez, S. Almeida, and D. Zubia, J. Appl. Phys. **120**, 045304 (2016).

[30] C. Wang, D. Smith, S. Tobin, T. Parodos, J. Zhao, Y. Chang, and S. Sivananthan, J. Vac. Sci. Technol. A **24**, 995–1000 (2006).

[31] A. G. Cullis, N. G. Chew, and J. L. Hutchison, Ultramicroscopy **17**, 203–211 (1985).

[32] W. J. Everson, C. K. Ard, J. L. Sepich, B. E. Dean, G. T. Neugebauer, and H. F. Schaake, J. Electron. Mater. **24**, 505–510 (1995).

[33] I. Hähnert and M. Schenk, J. Cryst. Growth **101**(1–4), 251–255 (1990).

[34] L. Burgess, F. J. Kumar, and J. Mackenzie, J. Electron. Mater. **44**, 3277–3282 (2015).

[35] J. Selvidge, J. Norman, E. T. Hughes, C. Shang, D. Jung, A. A. Taylor, M. J. Kennedy, R. Herrick, J. E. Bowers, and K. Mukherjee, Appl. Phys. Lett. **117**, 122101 (2020).

[36] M. A. Moram and M. E. Vickers, Rep. Prog. Phys. **72**, 036502 (2009).

[37]T. Hammerschmidt, P. Kratzer, and M. Scheffler, Phys. Rev. B **75**, 235328 (2007).
[38]J.-M. Wagner and F. Bechstedt, Phys. Rev. B **66**, 115202 (2002).
[39]H. J. McSkimin and D. G. Thomas, J. Appl. Phys. **33**, 56–59 (1962).
[40]B. H. Lee, J. Appl. Phys. **41**, 2988–2990 (1970).
[41]B. Yarlagadda, A. Rodriguez, P. Li, R. Velampati, J. F. Ocampo, E. N. Suarez, P. B. Rago, D. Shah, J. E. Ayers, and F. C. Jain, Appl. Phys. Lett. **92**, 202103 (2008).
[42]G. Zhao, L. Wang, S. Yang, H. Li, H. Wei, D. Han, and Z. Wang, Sci. Rep. **6**(1), 20787 (2016).